doi: 10.18323/2782-4039-2023-2-64-7

Microstructure and properties of the Zn–1%Li–2%Mg alloy subjected to severe plastic deformation

Vil D. Sitdikov*[1,2,4], Doctor of Sciences (Physics and Mathematics), expert
Elvira D. Khafizova[2,3,5], PhD (Engineering), assistant professor of Chair of Materials Science and Physics of Metals, senior researcher at the Research Laboratory "Metals and Alloys under Extreme Impacts"
Milena V. Polenok[2,3,6], graduate student, laboratory assistant of the Research Laboratory "Metals and Alloys under Extreme Impacts"
[1]*LLC RN-BashNIPIneft, Ufa (Russia)*
[2]*Institute of Physics of Molecules and Crystals of Ufa Research Center of the RAS, Ufa (Russia)*
[3]*Ufa University of Science and Technologies, Ufa (Russia)*

***E-mail: SitdikovVD@bnipi.rosneft.ru**

[4]ORCID: https://orcid.org/0000-0002-9948-1099
[5]ORCID: https://orcid.org/0000-0002-4618-412X
[6]ORCID: https://orcid.org/0000-0001-9774-1689

Received 29.05.2023 *Accepted 13.06.2023*

Abstract: In this paper, the authors consider the mechanisms of formation of high-strength states in the Zn–1%Li–2%Mg alloy as a result of its processing by the high pressure torsion (HPT) method. For the first time, the study showed that using HPT treatment, as a result of varying the degree of deformation at room temperature, it is possible to increase the ultimate strength of a zinc alloy from 155 to 383 MPa (with an increase in the yield stress from 149 to 306 MPa) without losing its ductility. To explain the reasons for the increase in the zinc alloy mechanical properties, its microstructure was analyzed by scanning electron microscopy (SEM), X-ray phase analysis (XPA), X-ray diffraction analysis (XRD), and small-angle X-ray scattering (SAXS). Using XPA, the authors established for the first time that $Zn_{(eutectic)}$+β-$LiZn_{4(eutectic)}$→~$LiZn_3$+$Zn_{(phase)}$+$Zn_{(precipitation)}$ and $MgZn_2$→Mg_2Zn_{11} phase transformations occur in the zinc alloy during HPT treatment. SEM analysis showed that at the initial stages of HPT treatment, cylindrical Zn particles with a diameter of 330 nm and a length of up to 950 nm precipitate in β-$LiZn_3$ phase. At the same time, the SAXS method showed that needle-like $LiZn_4$ particles with a diameter of 9 nm and a length of 28 nm precipitate in the Zn phase. The study established that, only spherical Zn and $LiZn_4$ particles precipitate at high degrees of HPT treatment. Precision analysis of the zinc alloy microstructure showed that HPT treatment leads to grain refinement, an increase in the magnitude of crystal lattice microdistortion, a growth of the density of dislocations, which are predominantly of the edge type. As a result of the analysis of hardening mechanisms, the authors concluded that the increase in the zinc alloy strength characteristics mainly occurs due to grain-boundary, dislocation, and dispersion hardening.

Keywords: Zn–1%Li–2%Mg alloy; phase transformations in zinc alloy; severe plastic deformation; X-ray scattering methods; strength and plasticity; deformation mechanisms.

Acknowledgements: The research was supported by the grant of the Russian Science Foundation No. 23-29-00667, https://rscf.ru/project/23-29-00667.

The paper was written on the reports of the participants of the XI International School of Physical Materials Science (SPM-2023), Togliatti, September 11–15, 2023.

For citation: Sitdikov V.D., Khafizova E.D., Polenok M.V. Microstructure and properties of the Zn–1%Li–2%Mg alloy subjected to severe plastic deformation. *Frontier Materials & Technologies*, 2023, no. 2. DOI: 10.18323/2782-4039-2023-2-64-7.

INTRODUCTION

Currently, zinc and its alloys demonstrate a high potential for industrial applications in medicine, due to their high biocompatibility and corrosion resistance [1–3]. As is known [4], pure Zn is a quite brittle material with low strength properties (yield strength is ~29 MPa, ultimate strength is ~34 MPa, ductility is ~1 %). Therefore, it needs significant strengthening to meet the clinical requirements for biodegradable metal stents (yield strength is >200 MPa, tensile strength is >300 MPa, ductility is >15–18 %) [5]. In order to improve the physical and mechanical properties of zinc and expand its application field in medicine, it is necessary to alloy it with certain biosoluble admixtures (lithium, magnesium, calcium, etc.), and carry out thermomechanical treatment according to various schemes and modes.

Among various classes of zinc alloys, the Zn–Li–Mg system is of particular interest, since, on the one hand, it is capable of aging, and, on the other hand, it has corrosion resistance and biocompatibility values close to pure zinc [3; 6; 7]. Under traditional modes of thermomechanical treatment (rolling + annealing), hardening in the Zn–Li system alloys occurs due to the precipitation of $LiZn_4$ particles in the Zn phase, and Zn particles in the primary β-$LiZn_4$ phase of predominantly acicular morphology, which, when intertwined, form a spatial grid [3; 6; 7]. This type of two-phase precipitation of particles during warm rolling allows increasing the ultimate strength of this alloy from 230 to 360 MPa [6]. In the recent work [8], the mechanical properties of Zn–0.8%Li, Zn–0.8%Li–0.2%Mg, and Zn–0.8%Li–0.2%Ag alloys were studied. The study showed that a Zn–Li–Ag system alloy has high ductility, and a Zn–Li–Mg

system alloy has the highest yield strength and tensile strength [8]. At the same time, by increasing the Mg content in the Zn–0.8%Li–0.4%Mg alloy and performing hot extrusion, the authors [1] showed that the alloy achieves a tensile strength of ~647 MPa, which is currently the maximum value.

Despite the relatively high hardness indices of the Zn–Li–Mg system alloys, an active search for new modes and schemes of thermomechanical treatment aimed at further increasing the strength properties of this alloy, is still carried out, since this issue remains very relevant. Recent studies demonstrate that an increase in strength properties in metals and alloys can be achieved by grinding the grain structure using severe plastic deformation (SPD) [9–11]. One should note that the grain structure refinement in zinc alloys has its own characteristics, since in thermally hardened zinc alloys, the aging processes are observed, which leads to the release of atypical hardening particles of the second phases [12]. This creates additional opportunities for improving the strength properties of zinc alloys; however, it requires optimization of technological modes for obtaining ultrafine-grained (UFG) samples, which simultaneously combine high biocompatibility, increased strength, and optimal corrosion rate. At the same time, new hardening mechanisms (segregations and nanoclusters) can also be involved in UFG metallic materials leading to an increase in the mechanical properties of metals and alloys. In this regard, it is important to comprehensively study the microstructure of the formed UFG Zn–Li–Mg alloys using various methods of X-ray phase analysis (XPA), X-ray diffraction analysis (XRD), electron microscopy, and small-angle X-ray scattering (SAXS).

The purpose of the study is to improve the strength characteristics of the Zn–1%Li–2%Mg zinc alloy as a result of SPD, as well as to identify possible hardening mechanisms explaining high-strength states.

METHODS

As an object of research, the biosoluble Zn–1.0 wt. % Li–2.0 wt. % Mg alloy made of high-purity components Zn (99.95 wt. %), Mg (99.95 wt. %), and Li (99.95 wt. %) was selected. To enhance strength characteristics and improve corrosion resistance, this alloy was subjected to high-pressure torsion (HPT) at room temperature with a number of revolutions equal to 0.5, 1, 2, 3, 6, 8 and 10. The pressure applied during HPT was 6 GPa, the rotation speed of the strikers was 1 rpm. Mechanical tensile tests of the alloy were carried out using a special-purpose testing machine for small samples, and the material microhardness was measured by the Vickers method on a Shimadzu HMV-G universal hardness tester with an indenter load of 100 g.

To determine the microstructure parameters using the XRD method, the authors analyzed the diffraction patterns obtained on a Bruker D8 Advance diffractometer (Bragg – Brentano scheme). The diffraction patterns were measured in the continuous shooting mode at a speed of 1.5 °/min within the scattering angle 2θ from 20° to 150° on $Cu_{K\alpha}$ radiation generated at a voltage of 40 kV and a current of 40 mA. The lattice constant, the size distribution of coherent scattering domains (CSD), the dislocation density, and the fraction of edge-type dislocations were determined using the PM2K program [13]. The diffraction patterns were analysed by refining such parameters as sample displacement in depth and angular position, lattice constant a, dislocation density ρ, fraction of edge-type dislocations m_{ixp}, effective dislocation radius R_e, shapes and sizes of CSD D.

Qualitative X-ray phase analysis was performed using the PDF-2 diffraction database in the EVAplus program (www.bruker.com). Quantitative X-ray phase analysis with determining the ratio of the identified phases was carried out by the Rietveld method [14] in the TOPAS v. 4.2 program (www.bruker.com). Scattering curves necessary to analysed the size and shape of precipitates were obtained on a Bruker D8 Advance diffractometer with a small-angle attachment in the parallel beam mode. Scattering curves were measured within the range of q vector from 0.0 to 1.5 nm^{-1}. The diameter of the analysed surface was ~4 mm.

The investigated alloy microstructure analysis was carried out by scanning electron microscopy (SEM) on a FEI Thermo Scientific Q250 scanning electron microscope. The main characteristics of the survey: accelerating voltage of electrons is 25 kV, beam diameter is 2 μm, focal length is 10.0 mm, pressure in the chamber is 5×10^{-4} Pa.

RESULTS

Results of measuring the mechanical properties

Table 1 shows the results of tests for measuring the zinc alloy microhardness and mechanical properties. The analysis of the results of tensile tests of samples showed that the alloy in the initial state is characterized by relatively low values of the yield strength, tensile strength and extremely low ductility, typical of the coarse-grained analogs of this alloy [3; 6]. HPT treatment leads to the expected growth of strength characteristics (Table 1). In particular, even at the initial HPT treatment stages (1–2 revolutions), the value of the yield strength increases by ~1.7 times, and the ultimate strength value increases by more than 2 times compared to the initial state. In this case, a sharp increase in ductility is observed. The increase in the alloy microhardness values is also in good agreement with the data of mechanical tests (Table 1).

When increasing the number of HPT revolutions from 3 to 6, a further, although insignificant, increase in the alloy strength characteristics is observed. The results after 10 HPT revolutions are the most interesting (Table 1). In this state, compared with the initial (as-cast) state, the microhardness value increases by more than 5 %, the ultimate strength increases by more than 2 times, and the ultimate strength increases by ~2.6 times.

Results of SEM studies

Fig. 1 shows the SEM images of the microstructure of the alloy in the initial (as-cast) state. The as-cast zinc alloy microstructure is characterized by bright and dark areas (Fig. 1 a–c), and two types of bright areas are distinguished (Fig. 1 a). The first type predominantly consists of an oval shape with an average diameter of 18 μm (Fig. 1 a). In some places, these areas merge into rather large areas. The second type of bright areas has a layered structure of different lengths (Fig. 1 b). The average layer width is 800 nm, and their length varies from one to several tens of microns. The analysis of the area of light regions showed that its surface fraction is ~88 %. As is known [3; 6], on the Li–Zn alloy phase

Table 1. *The values of microhardness and mechanical properties of the Zn–1%Li–2%Mg alloy*

State		HV	σ_T, MPa	σ_B, MPa	*e*, %
Initial		170.0±8.0	149	155	~0,4
HPT	**1 rev.**	183.8±12.8	256	383	42
	2 rev.	176.9±6.8	260	332	41
	3 rev.	176.7±12.0	264	361	44
	6 rev.	180.6±11.3	278	363	48
	8 rev.	179±12.6	301	394	51
	10 rev.	178.9±13.3	330	409	47

Note. HV – Vickers microhardness; σ_T – yield stress; σ_B – ultimate strength; e – percentage of elongation.

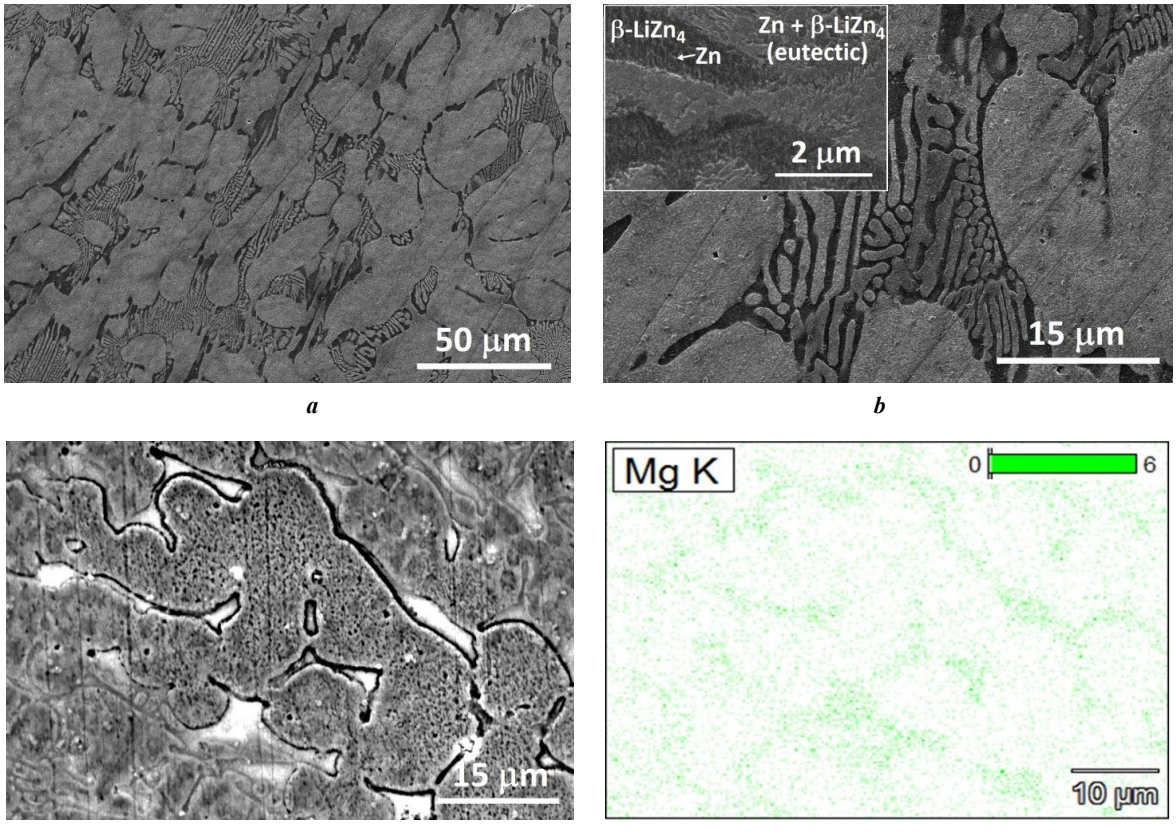

Fig. 1. *SEM images of the zinc alloy microstructure in the post-cast state at various magnifications:* ***a*** *– ×2000;* ***b*** *– ×8000, in the insert ×80000;* ***c*** *– ×6000;* ***d*** *– distribution of Mg atoms in Fig. 1 c*

diagram at a Zn content of about 97 %, one can expect the formation of the primary β-$LiZn_4$ phase, as well as the Zn and β-$LiZn_4$ eutectic phases. According to [6], lithium atoms have a much lower retarding potential, in contrast to zinc atoms. Considering the Li–Zn system phase diagram, it can be affirmed that the light (oval + layered) regions in the SEM images should belong to the Zn+β-$LiZn_4$ eutectic phases. At the same time, dark areas with a surface fraction of ~12 % should belong to the primary β-$LiZn_4$ phase.

Fig. 1 b and the insert show the precision areas of light and dark regions at high magnifications. During microstructure detailed analysis, one can see that there are numerous fine particles of predominantly acicular shape (Fig. 1 b, insert) in the primary β-$LiZn_4$ phase (dark areas). The average particle diameter is ~80 nm, and their length varies within 60–230 nm. According to the literature data [3; 6; 7], in the primary β-$LiZn_4$ phase, when the alloy is cooled, zinc particles usually precipitate (Fig. 1 b, insert). On the other

hand, the light areas belonging to the Zn+β-$LiZn_4$ phase have a lamellar structure typical of a eutectic (Fig. 1 b, insert). Since the dark areas are more subjected to etching corrosion processes, they can be identified in SEM images as β-$LiZn_4$ eutectic phases (Fig. 1 b).

Fig. 1 c shows an image atypical for the Zn–Li system alloy with many bright areas located mainly along the boundaries of the Zn+β-$LiZn_4$ eutectic and the primary β-$LiZn_4$ phase. To identify them, the authors carried out the element-by-element mapping, the result of which is shown in Fig. 1 d. A comparative analysis of the images (Fig. 1 c, 1 d) showed that the Mg atoms belonging to the $MgZn_2$ phase, as shown below by the XPA method, are concentrated in the detected bright areas.

Fig. 2 presents SEM images of the alloy after various degrees of HPT treatment. It is evident that during implementing the HPT treatment, even at the early stages of torsion (0.5 revolution), changes in the ratio of dark and bright areas are visible against the initial (as-cast) state (Fig. 2 a). It can be seen that, in the primary β-$LiZn_4$ phase (dark areas), filamentous zinc precipitates grow intensively with the formation of a peculiar network of precipitates (Fig. 2 a, insert). The analysis showed that the diameter of zinc precipitates varies from ~90 to ~785 nm, and their length varies from 110 nm to 10 μm. Moreover, at the boundary of the eutectic Zn+Mg_2Zn_{11} phase (bright areas, according to X-ray diffraction data presented below), a ~2 μm thick zinc phase is formed (Fig. 2 a, insert). The belonging of this layer to the zinc phase follows from the fact that there is no clear transition interface between this phase and zinc precipitates in the primary β-$LiZn_4$ phase. This fact confirms that these structures belong to the same phase.

When increasing the number of HPT rotations (1 revolution), a band (elongated) structure oriented perpendicular to the radius of the sample is formed (Fig. 2 b). Moreover, in the primary β-$LiZn_4$ phase, a certain orientation of zinc precipitates is visible, which sometimes merge (Fig. 2 b, insert). The images show that the thickness of the Zn+Mg_2Zn_{11} phase plates decreases even more.

It was noted that when increasing the number of HPT treatment revolutions, the proportion of dark areas increases, while the proportion of light areas decreases (Fig. 2 c, 2 d). High degrees of HPT treatment are characterised by effective grinding of the Zn+~$LiZn_3$ (~$LiZn_3$ phase is similar to β-$LiZn_4$) phase, as well as of the Zn+Mg_2Zn_{11} and Zn phases (Fig. 2 c, 2 d). In particular, it can be seen that the average grain size of the zinc phase is ~230 nm (Fig. 2 c, insert), which contain darkened areas related to $LiZn_4$ precipitates. In this case, the Zn precipitates themselves in the ~$LiZn_3$ phase precipitate in a spherical shape (Fig. 2 d, insert). The information found by the microscopy method indicates the intense phase transitions and changes that have occurred in certain phases. In particular, by increasing the proportion of dark areas and XPA results, it is possible to identify the $Zn_{(eutectic)}$+β-$LiZn_{4(eutectic)}$→~$LiZn_3$+$Zn_{(phase)}$+ +$Zn_{(precipitate)}$+Mg_2Zn_{11}+β-$LiZn_4$ phase transition.

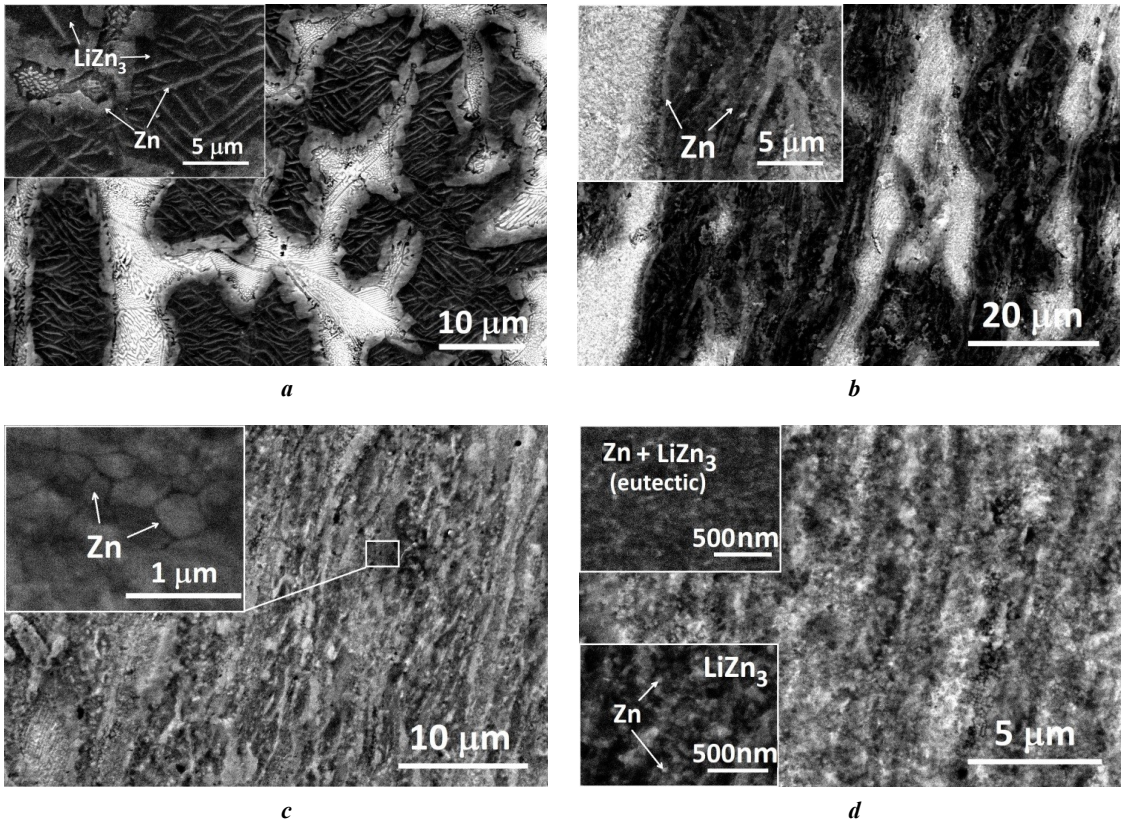

Fig. 2. *SEM images of the zinc alloy microstructure in the state after HPT treatment:*
a *– 0.5 revolution, in the insert – Zn particles and Zn phase;* ***b*** *– 1 revolution, in the insert – Zn particles;*
c *– 6 revolutions, in the insert – Zn grains;* ***d*** *– 10 revolutions, in the inserts – Zn particles*

Results of studies by XRD analysis

Fig. 3 shows the X-ray spectra of the studied states and an example of the processed section of the zinc alloy diffraction pattern. The analysis of the general view of the diffraction patterns showed that all zinc alloy X-ray spectra are characterised by the same set of intense peaks (Fig. 3 a). At the same time, qualitative XPA showed that the detected reflections belong to the Zn, ~$LiZn_3$, β-$LiZn_4$, $MgZn_2$, and Mg_2Zn_{11} phases (Fig. 3 b). The analysis of the diffraction patterns showed that the original alloy reflections are quite narrow, and HPT treatment leads both to a broadening of the reflections and to a quantitative change in the ratio of reflection intensities (Fig. 3).

The peculiarities found on the diffraction patterns indicate changes in the identified phases and the occurrence of various phase transitions in the studied alloy as a result of HPT treatment. To determine the quantitative characteristics of phase transitions, the authors analysed the diffraction patterns using the Rietveld method implemented in the TOPAS program. An example of processing the alloy diffraction pattern measured after HPT (1 revolution) is shown in Fig. 3 b. It should be noted that in all the studied

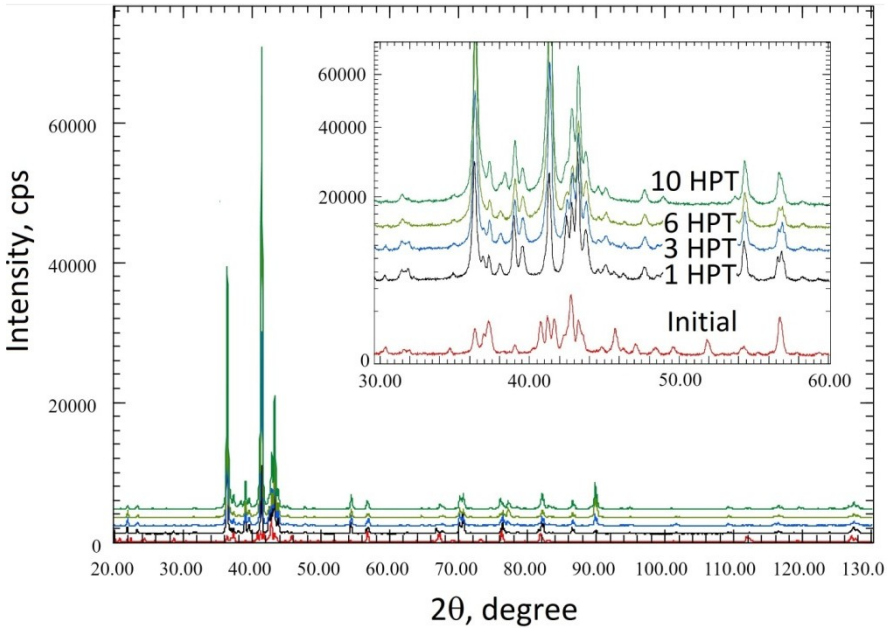

a

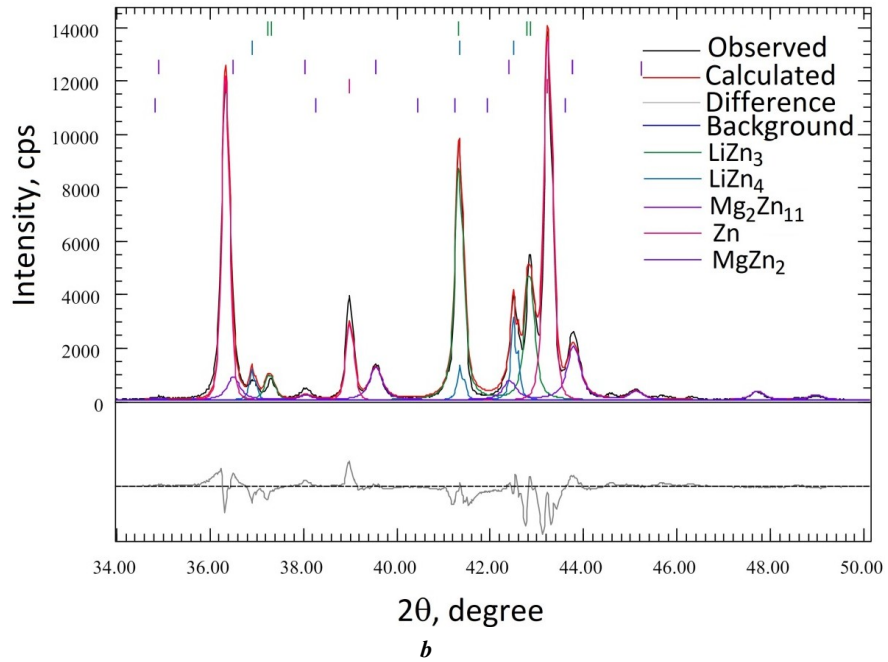

b

Fig. 3. *Diffraction patterns of the Zn–Li–Mg alloy in the initial state and after HPT treatment:* ***a*** *– general view of diffraction patterns, in the insert – precision surveying area from 30° to 60°;* ***b*** *– a section of the diffraction pattern processed by the Rietveld method*

states, the diffraction patterns were refined until a value of less than 5 %, and the permissible limit of the χ^2 value was set equal to 1.5 %. The results of qualitative and quantitative phase analyses for the selected states are shown in Tables 2–4.

The analysis of the zinc alloy in the initial (as-cast) state showed that the β-$LiZn_4$, ~$LiZn_3$, $MgZn_2$, and Zn phases were formed in it. Their quantitative ratio is given in Table 2. In the initial state of the alloy, the main phase includes the β-$LiZn_4$+Zn eutectic phase (~76 %), i.e., light areas detected by SEM. To assess the correctness of XPA calculations, the detected phases were first decomposed into elemental components in terms of Zn, Li, and Mg (Table 2), and then their total values were compared with the casting data (Table 1, bottom row).

The XPA obtained results are in very good agreement with the data obtained when casting the blank parts. This fact indicates the XPA correctness and obtaining correct information about the quantitative ratio of the phases. In the case of HPT treatment applied to the alloy, the mass fractions of the β-$LiZn_4$, ~$LiZn_3$, and $MgZn_2$ phases decrease, while the zinc fraction increases (Table 3). At the same time, HPT treatment leads to the formation of the Mg_2Zn_{11} phase, which is non-characteristic of the as-cast state, i.e., to the occurrence of the $MgZn_2 \rightarrow Mg_2Zn_{11}$ phase transition. An increase in the number of revolutions of the HPT treatment leads to a further regular growth of the Zn and Mg_2Zn_{11} phases (Table 3). In this case, a slight decrease in the content of the β-$LiZn_4$, ~$LiZn_3$, and $MgZn_2$ phases are observed.

A precision analysis of the diffraction patterns showed that, in contrast to the diffraction pattern of the initial state, the measured X-ray spectra of HPT samples are characterised both by a redistribution of reflection intensity and by an increased width of diffraction maxima. As a rule, an increase in the width of reflections characterises the changes occurred in the analyzed material microstructure, and, first of all, they are associated with a decrease in the CSD size, an increase in the crystal lattice microdistortions, and the density of introduced defects.

To assess these changes, the authors performed a full-profile analysis of the diffraction patterns in the PM2K program. When analysing, the main attention was paid to the Zn phase, since its content during HPT treatment is maximum. The data on the alloy microstructural characteristics obtained as a result of the XRD analysis of the diffraction patterns are shown in Table 4.

Fig. 4 shows the CSD size distributions in the phase of zinc in the initial state and in the states after HPT treatment. In the initial state, the average CSD size is typical for coarse-grained metallic materials (~380 nm). The implementation of 1 HPT revolution leads to a significant decrease in the CSD size to 86 nm (Fig. 4, Table 5). With a further increase in the number of HPT revolutions, a regular decrease in the CSD size to ~30 nm is observed (Fig. 4). At high HPT degrees, the CSD average size scarcely changes.

Results of SAXS studies

Fig. 5 shows the scattering curves measured on thin foils of the original alloy and the alloy after HPT, as well as the results of their processing. The SAXS curve of the initial state is characterised by one inflection. After HPT treatment, the scattering curves have two inflection points, one of which is concentrated in the region of small values of the scattering vector q, and the other is located in the region of large q values (Fig. 5 a). This fact indicates the presence of precipitates of one type in the initial state and two types (small and large) of precipitates after HPT, i.e., the bimodal nature of the particle distribution.

The inflection on the SAXS curve of the initial state is located in the region from 0.4 to 0.6 nm^{-1}, and the type of the intensity dependence decreases according to $I(1/q^2)$. According to [16; 17], this indicates the precipitation of cylindrical particles. After HPT treatment of zinc alloy, the general view of the SAXS curve changes (Fig. 5 a). In particular, after 1 HPT revolution, two inflection sections can be distinguished on the SAXS curve. The first inflection is concentrated in the range up to 0.15 nm^{-1}, and before the inflection, the intensity decreases according to the $I(1/q^2)$ dependence (Fig. 5 a), which indicates the precipitation of relatively large cylindrical precipitates [16; 17]. The second inflection section on the SAXS curve is in the range from 0.75 to 0.85 nm^{-1}, and the X-ray quanta intensity decreases according to the $I(1/q^4)$ dependence. Such a dependence on the SAXS curve manifests itself during intensity decreases according to the $I(1/q^4)$ dependence. Such a dependence on the SAXS curve manifests itself during the precipitation of spherical particles [16; 17]. When increasing the number of HPT treatment revolutions, the first

Table 2. *The detected phases, their weight fractions and element-by-element content of Zn, Li, and Mg atoms in each component. Initial (as-cast) state*

Phases	Phase fraction, wt. %	Element content in the phase, wt. %		
		Li	Mg	Zn
β-$LiZn_4$	11.85	2.59	0.00	97.41
β-$LiZn_4$ (eut.)	44.98	1.30	0.00	98.70
Zn	31.31	0.35	0.45	99.20
$MgZn_2$	11.86	0.00	15.67	84.33
Total	100.00	1.00	2.00	97.00

Table 3. *The detected phases, their weight fractions and element-by-element content of Zn, Li, and Mg atoms in each component. HPT treatment (1 revolution)*

Phases	Phase fraction, wt. %	Element content in the phase, wt. %		
		Li	Mg	Zn
β-$LiZn_4$	9.65	2.59	0.00	97.41
~$LiZn_3$	24.43	2.66	0.00	97.34
Mg_2Zn_{11}	16.28	0.00	6.33	93.67
Zn	47.65	0.21	1.38	98.41
$MgZn_2$	1.99	0.00	15.67	84.33
Total	100.00	1.00	1.99	97.01

Table 4. *The detected phases, their weight fractions and element-by-element content of Zn, Li, and Mg atoms in each component. HPT treatment (10 revolutions)*

Phases	Phase fraction, wt. %	Element content in the phase, wt. %		
		Li	Mg	Zn
β-$LiZn_4$	7.23	2.59	0.00	97.41
~$LiZn_3$	21.66	3.47	0.00	96.53
Mg_2Zn_{11}	18.24	0.00	6.33	93.67
Zn	52.39	0.12	1.47	98.41
$MgZn_2$	0.48	0.00	15.67	84.33
Total	100.00	1.00	1.99	97.01

and second inflection points shift towards small vector q values (Fig. 5 a), which is associated with the size growth of precipitates.

The analysis of the SAXS curves showed that, in the initial state, Zn precipitates in the β-$LiZn_4$ phase precipitate in an acicular shape with an average diameter of 75 nm and a length of 150 nm (Fig. 5 b). As a result of HPT treatment (1 revolution), in addition to Zn particles, β-$LiZn_4$ particles also precipitate in the alloy; however, in contrast to the initial state, they have different shapes and sizes. Large particles after 1 HPT revolution, related to Zn precipitates, have a cylindrical shape with a diameter of 330 nm and a length of up to 900 nm. At the same time, small particles belong to $LiZn_4$ precipitates and are formed in a spherical shape with a diameter of 17 nm (Fig. 5 b).

When increasing the number of HPT revolutions, regular changes in the particle size and morphology are observed. In particular, after 10 HPT revolutions, only spherical morphology is formed. In this case, the average size of small $LiZn_4$ particles is 45 nm, while larger Zn particles have an average diameter of 86 nm.

DISCUSSION

The results of tensile tests of the specimens factually demonstrated a significant increase in the zinc alloy mechanical properties during HPT treatment. In particular, the analysis of the results of mechanical tests showed that even after 1 HPT treatment revolution, the yield strength increases by ~1.7 times, and the ultimate strength increases by about 2.5 times (Table 1). With a further increase in the HPT treatment degree, a regular increase in mechanical properties occurs (Table 1). After 10 HPT revolutions implemented at room temperature, the yield stress of 330 MPa and tensile strength of 409 MPa, maximum for this alloy, were found. To explain the obtained record values of mechanical properties and to analyze possible hardening mechanisms, the alloy microstructure analysis was carried out.

The conducted studies using microscopy and X-ray diffraction analysis showed that in the Zn–1%Li–2%Mg alloy during HPT treatment, phases of the same type are formed with the precipitates identical in type (Fig. 1, 2). As known [3; 6], as the casting temperature drops to room temperature, according to the phase diagram, the solubility of Zn atoms in the β-$LiZn_4$ phase decreases, therefore,

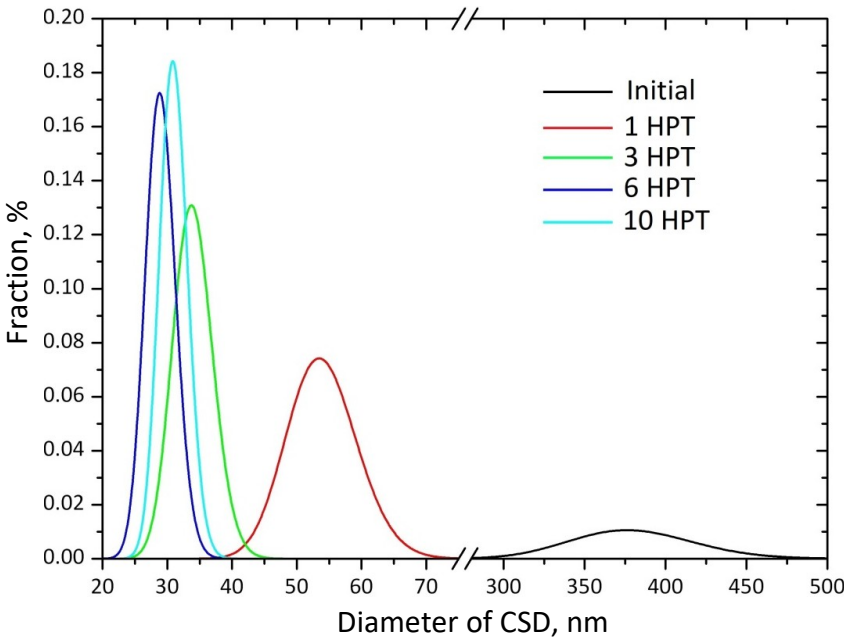

Fig. 4. *CSD distribution by sizes in the alloy in the initial state and after different HPT treatment degrees*

Table 5. *Parameters of the zinc alloy microstructure obtained by the XRD method*

State	*a/c*, nm	D_{ave}, nm	D_{SEM}, nm	ε, %	ρ, 10^{15} m^{-2}	m_{ixp}, %
Initial	0.266123 0.493885	370±80	60000	0.08±0.01	0.5±0.1	0.29±0.03
HPT, 1 rev.	0.266604 0.494040	86±4	906	0.15±0.01	2.4±0.2	0.41±0.02
HPT, 3 rev.	0.266578 0.494251	43±1	383	0.23±0.01	5.1±0.1	0.68±0.03
HPT, 6 rev.	0.266595 0.494252	29±2	246	0.26±0.01	5.4±0.1	0.79±0.02
HPT, 10 rev.	0.266588 0.494254	32±3	218	0.25±0.02	5.3±0.4	0.77±0.04

Note. a/c – lattice constant, pure zinc: a/c=0.26594/0.49368 [15];
D_{ave} – average dimension of CSD obtained by the XRD method;
D_{SEM} – grain dimension obtained by SEM;
ε – RMS crystal lattice microdistorsion;
ρ – density of dislocations;
m_{ixp} – the proportion of edge-type dislocations.

Zn particles will precipitate in the β-$LiZn_4$ phase. On the other hand, the solubility of Li atoms in the Zn phase also sharply decreases upon cooling, which leads to the formation of β-$LiZn_4$ precipitates in the Zn phase. In the initial state, the zinc alloy is characterised by the presence of a primary β-$LiZn_4$ phase, a Zn+β-$LiZn_4$ eutectic phase, and a $MgZn_2$ phase. In this case, as the analysis showed, Zn particles of cylindrical morphology precipitate in the β-$LiZn_4$ phase. For the quantitative characteristics of the detected phases, the authors analysed the diffraction patterns using the Rietveld method. To check the correctness of the quantitative XPA results, the content of each phase was decomposed into elemental components (Table 2) and compared with the data taken during alloy casting.

The comparison of the total content of Zn, Li, and Mg atoms with the data entered during the casting of blank parts showed a very good convergence between them. This fact indicates the reliability of the information obtained in the ratio of the analysed phases. In particular, XPA shows that in the initial state, the mass content of Li atoms in the primary β-$LiZn_4$ phase is 2.59 %, and the content of Zn atoms is 97.41 %, which corresponds to the equilibrium

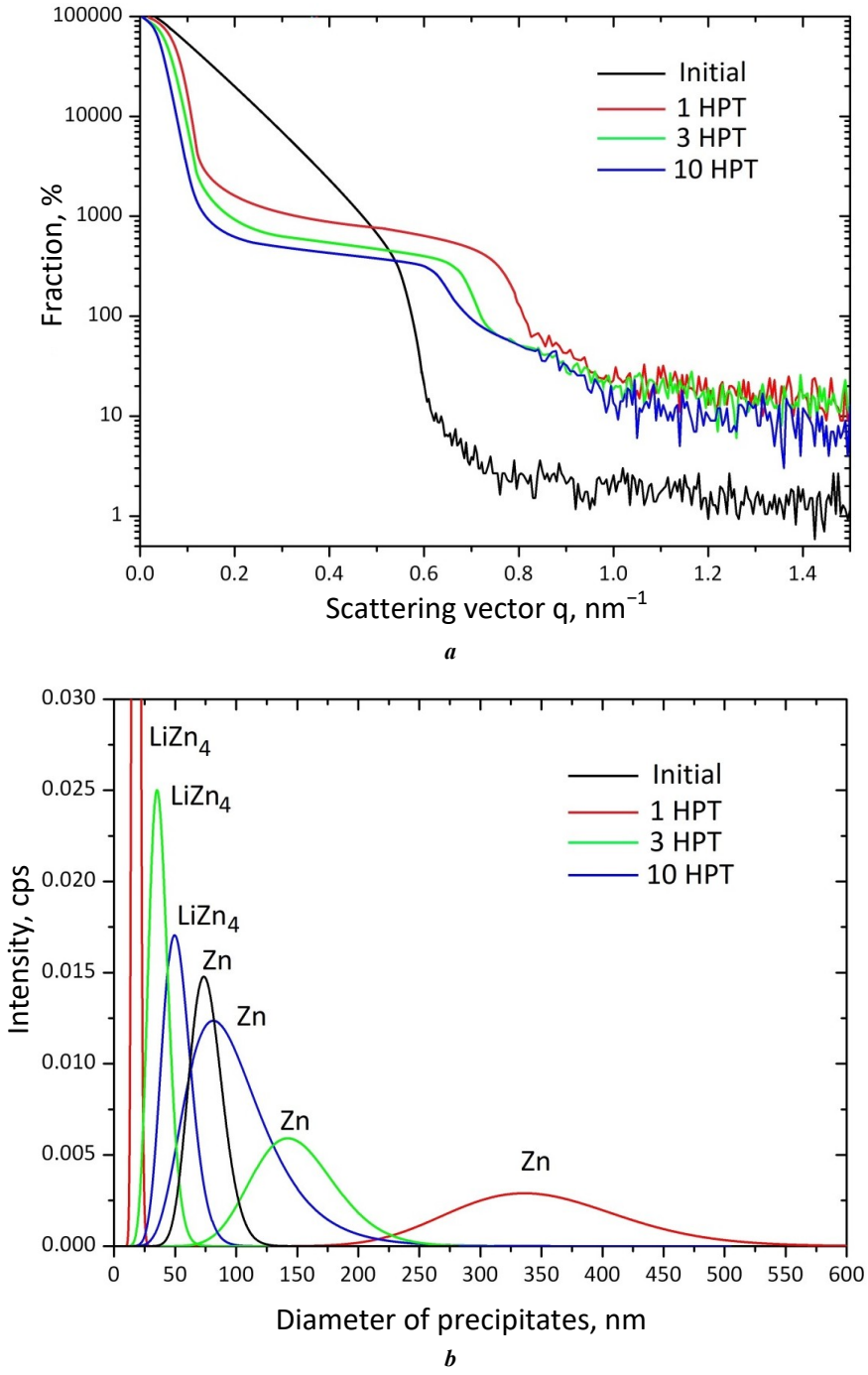

Fig. 5. *Data of small-angle X-ray scattering (SAXS) of the alloy in different structural states:* ***a*** *– SAXS curves;* ***b*** *– precipitation distribution*

state of this component. At the same time, in the $LiZn_4$ eutectic phase, a reduced content of Li atoms (1.30 %) compared with the standard value of 2.59 % in the primary β-$LiZn_4$ phase was revealed (Table 2). Moreover, a small content of Li and Mg atoms was found in the pure Zn phase, the presence of which led to an increase in the Zn lattice constant both along the *a* edge and along the *c* axis of the HCP lattice basis (Table 5). The total mass content of Li, Mg, and Zn atoms over all the phases taken in the zinc alloy is 1 %, magnesium is ~2 %, and zinc is ~97 % (Table 1, bottom line), which corresponds to the data taken during casting of the alloy.

The HPT treatment leads to significant changes in the quantitative ratios of the β-$LiZn_4$, ~$LiZn_3$, $MgZn_2$, and Zn phases in the alloy. In particular, at the HPT initial stages, the content of the ~$LiZn_3$ phase sharply decreases from ~45 to ~24 %. The content of Li atoms in this phase is higher than in the primary β-$LiZn_4$ phase; therefore, the β-$LiZn_4$ phase was defined as ~$LiZn_3$ [18]. This state is characterised by an increase in the proportion of the Zn phase from ~31 to ~48 %. Along with this, the fraction of Li atoms in the Zn phase decreases, while the fraction of Mg atoms increases (Table 3). The decrease in Li atoms in the Zn phase is most likely associated with the precipitation

of $LiZn_4$ particles, and an increase in the fraction of Mg atoms in the Zn phase leads to an increase in the Zn lattice constant (Table 5). As a result of HPT, the $MgZn_2 \rightarrow$ $\rightarrow Mg_2Zn_{11}$ phase transition atypical for the coarse-grained state also occurs (Table 3). With a further increase in the degree of HPT treatment, on the one hand, a further decrease in the content of the β-$LiZn_4$, ~$LiZn_3$, $MgZn_2$ phases, and, on the other hand, an increase in the proportion of the Zn and Mg_2Zn_{11} phases are observed. Moreover, it was found that the content of admixture Li atoms in the ~$LiZn_3$ phase increases, while the fraction of Mg atoms in the Zn phase increases, and the fraction of Li atoms decreases. These facts seem to indicate the precipitation of Zn particles in the ~$LiZn_3$ phase and the growth of β-$LiZn_4$ precipitates in the Zn phase. An increase in the content of Mg atoms in Zn leads to a further increase in the Zn lattice distance (Table 5).

The SEM studies factually confirmed the occurrence of the detected phase transformations. In particular, in the initial state, the SEM method revealed light areas (oval + layered) belonging to the Zn+β-$LiZn_4$ eutectic phase with a surface fraction of ~88 %, and dark areas with a fraction of ~12 % identified as the primary β-$LiZn_4$ phase (Fig. 1). At high magnifications, in the primary β-$LiZn_4$ phase, numerous acicular Zn precipitates with a diameter of ~80 nm and a length from 60 to 230 nm were identified. The dimensions of these precipitates agree with the results of SAXS studies (Fig. 5 b). During HPT treatment, significant changes occur in the microstructure. The SEM images of the alloy (0.5 HPT revolution) show predominantly dark areas (Fig. 2 a). This fact is associated with an increase in the content of Li atoms in the ~$LiZn_3$ phase (Table 3) and taking into account the low retarding potential of Li (–3.04 V) compared to Zn (–0.76 V). The ~$LiZn_3$ phase is more subjected to etching, i.e., to the appearance of dark regions. At the early HPT stages (0.5 revolution), a decrease in the thickness of the bands of the Zn+Mg_2Zn_{11} phase to ~16 μm was revealed. In this case, the formation of the zinc phase around the eutectic phases was identified (Fig. 2 a). With an increase in the number of HPT revolutions to 1, the average thickness of the light plates decreases to ~11 μm, and after 10 HPT revolutions, its value decreases to 1.7 μm. Filamentous Zn precipitates generate in the $LiZn_4$ phase forming a grid of precipitates. The average diameter of Zn precipitates is 350 nm, and the average length is ~2 μm. Moreover, in this state, a band structure is formed, in which Zn precipitates are sometimes merge (Fig. 2 b, insert).

In general, with an increase in the degree of HPT treatment, an effective structure refinement occurs, and Zn precipitates have a spherical shape. The size and morphology of Zn precipitates detected by the SEM method correlate well with the results of SAXS studies (Fig. 5 b). In particular, the bimodal nature of the distribution of precipitates was established from the *I(q)* dependence of the scattering curve. In the early HPT stages, Zn precipitates have a cylindrical shape with a diameter of 330 nm and a length of up to 900 nm, while fine $LiZn_4$ particles precipitate in a spherical shape with an average diameter of 17 nm. When increasing the number of HPT revolutions to 10, the diameter of spherical $LiZn_4$ particles increases to 45 nm, and Zn precipitates have a spherical morphology and a diameter of 88 nm.

To assess the change in the microstructure parameters (CSD size, crystal lattice microdistortions, density and type of dislocations), the authors analysed the diffraction patterns using the PM2K program. The main attention was paid to the Zn phase, since it is the main phase in HPT treatment. The analysis showed that the application of HPT to the alloy leads to the CSD fragmentation (Fig. 4, Table 5). In particular, after 0.5 revolution, the average CSD size decreases from 410 to 86 nm. At the same time, lattice microdistortions and dislocation density sharply increase (Table 5). An increase in the degree of HPT treatment leads to further CSD refinement, an increase in microdistortions and defect density (Table 5). The analysis showed that dislocations at high degrees of HPT treatment are predominantly of the edge type, since the value of m_{ixp} is close to unity (Table 5).

The conducted studies of the alloy microstructure make it possible to assess qualitatively the main mechanisms responsible for its hardening. As possible hardening mechanisms, the authors considered grain boundary strengthening, solid solution strengthening, precipitation strengthening, and dislocation strengthening. In particular, the grain structure refinement (i.e., a decrease in the CSD) causes grain boundary strengthening σ_{gb} of the alloy, which can be determined by the Hall – Petch–type relationship [19]. The solid solution strengthening σ_{ss} of a supersaturated alloy solid solution will be determined by the excess content of Zn, Mg, and Li elements in the identified phases [20]. Precipitation strengthening σ_{pp} [21] is determined by the presence of precipitates and their proportions and is determined by the Ashby – Orowan relation, and the value of dislocation strengthening σ_d is directly proportional to $\sqrt{\rho}$ [22].

The obtained qualitative results of theoretical strength calculations are shown in Table 6, and give a visual representation of the expected contribution of each of the hardening mechanisms to the resulting strength of the alloy. It is obvious that in the initial state, the alloy strength is mainly provided by the mechanisms of dislocation and solid solution hardening (Table 6).

Table 6. *Contribution of different mechanisms to the alloy hardening*

State	σ_o	σ_{gb}	σ_{pp}	σ_d	σ_{ss}
Initial	+	+	+	++	++
After HPT	+	+++	+++	+++	+

In this case, the role of grain boundary and precipitation strengthening is low, which is explained by the rather large grain size (about 60 μm) and a small fraction of dispersed particles in the alloy structure. In the case of the HPT treatment implementation, the role of the grain boundary and dislocation strengthening mechanisms increases significantly, and the mechanisms of precipitation strengthening are also activated (Table 6). Thus, grain refinement,

an increase in the density of introduced defects, and an increase in the proportion of particles of secondary phases (Zn, $LiZn_4$) contributed significantly to the increase in the strength characteristics of the zinc alloy. At the same time, the increase in the alloy ductility during HPT is explained by the formation of a unique microstructure consisting of Zn and ~$LiZn_3$ phases, in which precipitates of different types and shapes simultaneously occur [3; 6].

CONCLUSIONS

As a result of processing by severe plastic deformation by torsion in the Zn–1%Li–2%Mg alloy, a high-strength state was obtained, characterised by a yield strength of 330 MPa and a tensile strength of 409 MPa. For the first time, the XPA method identified the occurrence of phase transformations during HPT: $Zn_{(eutectic)}$+β-$LiZn_{4(eutectic)}$→ →~$LiZn_3$+$Zn_{(phase)}$+$Zn_{(precipitate)}$+β-$LiZn_4$ and $MgZn_2$→ →Mg_2Zn_{11}. The study shows that HPT treatment leads to the formation of Zn precipitates in the ~$LiZn_3$ phase, as well as to the formation of β-$LiZn_4$ precipitates in the Zn phase. According to the results of SAXS studies, it was found that large Zn precipitates at the initial stages of HPT precipitate in a cylindrical shape, while small ones precipitate in a spherical shape. When increasing the degree of HPT treatment, zinc and $LiZn_4$ particles precipitate only in a spherical shape. Based on the analysis of diffraction patterns, it was found that HPT treatment leads to refinement of coherent scattering domains (grains), an increase in the crystal lattice microdistortions, and an increase in the density of dislocations, predominantly of the edge type. An increase in the alloy strength characteristics occurs due to grain refinement, an increase in the density of introduced defects, as well as an increase in the proportion of Zn and $LiZn_4$ precipitates.

REFERENCES

1. Yang H., Jia B., Zhang Z., Qu X., Li G., Lin W., Zhu D., Dai K., Zheng Yu. Alloying design of biodegradable zinc as promising bone implants for load-bearing applications. *Nature Communications*, 2020, vol. 11, no. 1, article number 401. DOI: 10.1038/s41467-019-14153-7.
2. Jia B., Yang H., Han Yu., Zhang Z., Qu X., Zhuang Y., Wu Q., Zheng Yu., Dai K. In vitro and in vivo studies of Zn-Mn biodegradable metals designed for orthopedic applications. *Acta Biomaterialia*, 2020, vol. 108, pp. 358–372. DOI: 10.1016/j.actbio.2020.03.009.
3. Li Z., Shi Z.-Z., Hao Y., Li H.-F., Liu X.-F., Volinsky A.A., Zhang H.-J., Wang L.-N. High-performance hot-warm rolled Zn-0.8Li alloy with nano-sized metastable precipitates and sub-micron grains for biodegradable stents. *Journal of Materials Science and Technology*, 2019, vol. 35, no. 11, pp. 2618–2624. DOI: 10.1016/j.jmst.2019.06.009.
4. Tong X., Zhang D., Zhang X. et al. Microstructure, mechanical properties, biocompatibility, and in vitro corrosion and degradation behavior of a new Zn–5Ge alloy for biodegradable implant materials. *Acta Biomaterialia*, 2018, vol. 82, pp. 197–204. DOI: 10.1016/j.actbio.2018.10.015.
5. Bowen P.K., Drelich J., Goldman J. Zinc Exhibits Ideal Physiological Corrosion Behavior for Bioabsorbable Stents. *Advanced materials*, 2013, vol. 25, pp. 2577–2582. DOI: 10.1002/adma.201300226.
6. Li Z., Shi Z.-Z., Hao Y., Li H.-H., Zhang H.-J., Liu X.-F., Wang L.-N. Insight into role and mechanism of Li on the key aspects of biodegradable Zn-Li alloys: Microstructure evolution, mechanical properties, corrosion behavior and cytotoxicity. *Materials Science and Engineering C*, 2020, vol. 114, article number 111049. DOI: 10.1016/j.msec.2020.111049.
7. Sitdikov V.D., Kulyasova O.B., Sitdikova G.F., Islamgaliev R.K., Yufeng Zh. Structural-phase transformations in the Zn-Li-Mg alloy exposed to the severe plastic torsion deformation. *Frontier Materials & Technologies*, 2022, vol. 3-2, pp. 44–55. DOI: 10.18323/2782-4039-2022-3-2-44-55.
8. Zhang Y., Yan Y., Xu X., Lu Y., Chen L., Li D., Dai Y., Kang Y., Yu K. Investigation on the microstructure, mechanical properties, in vitro degradation behavior and biocompatibility of newly developed Zn-0.8%Li-(Mg, Ag) alloys for guided bone regeneration. *Materials Science and Engineering: C*, 2019, vol. 99, pp. 1021–1034. DOI: 10.1016/j.msec.2019.01.120.
9. Martynenko N., Anisimova N., Rybalchenko O. et al. Structure, Biodegradation, and In Vitro Bioactivity of Zn–1%Mg Alloy Strengthened by High-Pressure Torsion. *Materials*, 2022, vol. 15, article number 9073. DOI: 10.3390/ ma15249073.
10. Mollaei N., Fatemi S.M., Abootalebi M., Razavi H. Zinc based bioalloys processed by severe plastic deformation - A review. *Journal Ultrafine Grained Nanostructure Materials*, 2020, vol. 53, pp. 39–47. DOI: 10.22059/JUFGNSM.2020.01.06.
11. Ye L., Liu H., Sun C., Zhuo X., Ju J., Xue F., Bai J., Jiang J., Xin Y. Achieving high strength, excellent ductility, and suitable biodegradability in a Zn-0.1Mg alloy using room-temperature ECAP. *Journal of Alloys Compounds*, 2022, vol. 926, article number 166906. DOI: 10.1016/j.jallcom.2022.166906.
12. Chen C., Fan S., Niu J., Huang H., Jin Z., Kong L., Zhu D., Yuan G. Alloying design strategy for biodegradable zinc alloys based on first-principles study of solid solution strengthening. *Materials & Design*, 2021, vol. 204, article number 109676. DOI: 10.1016/j.matdes.2021.109676.
13. Leoni M., Confente T., Scardi P. PM2K: A flexible program implementing Whole Powder Pattern Modelling. *Zeitschrift für Kristallographie, Supplement*, 2006, vol. 1, no. 23, pp. 249–254. DOI: 10.1524/9783486992526-043.
14. Rietveld H.M. A profile refinement method for nuclear and magnetic structures. *Journal of Applied Crystallography*, 1969, vol. 2, no. 2, pp. 65–71. DOI: 10.1107/S0021889869006558.
15. Jette E.R., Foote F. Precision determination of lattice constants Locality: synthetic Sample: at T = 25 C Note: lattice parameter is average of three samples. *Journal of Chemical Physics*, 1935, vol. 3, pp. 605–616. DOI: 10.1063/1.1749562.
16. Boldon L., Laliberte F., Liu L. Review of the fundamental theories behind small angle X-ray scattering, molecular dynamics simulations, and relevant integrated application. *Nano Review*, 2015, vol. 6, article number 25661. DOI: 10.3402/nano.v6.25661.
17. Pedersen J.S. Analysis of small-angle scattering data from colloids and polymer solutions: modeling and

least-squares fitting. *Advances in Colloid and Interface Science*, 1997, vol. 70, pp. 171–210. DOI: 10.1016/s0001-8686(97)00312-6.

18. Pavlyuk V., Chumak I., Akselrud L., Lidin S., Ehrenberg H. $LiZn_{4-x}$ (x=0.825) as a (3+1)-dimensional modulated derivative of hexagonal close packing. *Acta Crystallographica*, 2014, vol. 70, pp. 212–217. DOI: 10.1107/S2052520613030709.
19. Bednarczyk W., Wątroba M., Kawałko J., Bała, P. Can zinc alloys be strengthened by grain refinement? A critical evaluation of the processing of low-alloyed binary zinc alloys using ECAP. *Materials Science and Engineering: A*, 2019, vol. 748, pp. 357–366. DOI: 10.1016/j.msea.2019.01.117.
20. Bednarczyk W., Wątroba M., Jain M., Mech K., Bazarnik P., Bała P., Michler J., Wieczerzak K. Determination of critical resolved shear stresses associated with <a> slips in pure Zn and Zn-Ag alloys via micro-pillar compression. *Materials & Design*, 2023, vol. 229, article number 111897. DOI: 10.1016/j.matdes.2023.111897.
21. Lee J.D., Niessen P. Superplasticity in a new dispersion strengthened zinc alloy. *Metallurgical Transactions*, 1973, vol. 4, pp. 949–957. DOI: 10.1007/BF02645595.
22. Zhao C., Chen X., Pan F., Wang J., Gao S., Tu T., Liu C., Yao J., Atrens A. Strain hardening of as-extruded Mg-xZn (x = 1, 2, 3 and 4 wt%) alloy. *Journal of Materials Science & Technology*, 2019, vol. 35, no. 1, pp. 142–150. DOI: 10.1016/j.jmst.2018.09.015.